ENHANCED PHOTOCATALYTIC PERFORMANCE OF TITANIA NANOBELTS DECORATED WITH GOLD PARTICLES SYNTHESIZED USING STIRRING-ASSISTED HYDROTHERMAL METHOD

by

YI SHEN

Presented to the Faculty of the Graduate School of

The University of Texas at Arlington in Partial Fulfillment

of the Requirements

for the Degree of

MASTER OF SCIENCE IN MATERIALS SCIENCE AND ENGINEERING

THE UNIVERSITY OF TEXAS AT ARLINGTON

MAY 2015

Acknowledgements

At first, I wish to express my sincere thanks to my supervisor, Dr. Fuqiang Liu for the opportunities he offered me to do researches under his instruction. He provided not only useful advices but also continuous encouragement during the previous two years, which helped me overcome all difficulties that I met. The thesis would not be completed without all his effort. I also appreciate the financial support he offered me.

I am also grateful to Dr. Desheng Meng and Dr. Kyung Suk Yum for being my committee member and give me valuable suggestions to improve my future work. I would like to thank Dr. Chia-jen Hsu for all his help during my research. I wish to express my thanks to all other group members in Electrochemical Energy Lab for what they have done for me. I also appreciate the Department of Materials Science and Engineering and CCMB for the support to my research.

Finally, I would like to take the opportunity to express my thanks to my father Zihui and my mother Qingling for all their encouragement and love. I could not be more grateful to them.

April 20, 2015

Abstract

ENHANCED PHOTOCATALYTIC PERFORMANCE OF TITANIA NANOBELTS DECORATED WITH GOLD PARTICLES SYNTHESIZED USING STIRRING-ASSISTED HYDROTHERMAL METHOD

Yi Shen, M.S.

The University of Texas at Arlington, 2015

Supervising Professor: Fuqiang Liu

In this thesis, anatase TiO_2 nanobelts (TNBs) have been successfully obtained via an optimized stirring-assisted hydrothermal synthesis. The impact of stirring speed has been studied. Difference in morphology caused by stirring speed was observed by high resolution Field-Emission SEM (FE-SEM). Methylene Blue degradation test indicated that at certain stirring speed, i.e., 700 rpm, which was the highest, produced the best photoactivity than commercial P25 TiO_2.

Furthermore, Au decorated TNBs were obtained by a simple reduction reaction with Au-containing precursor. The Au-TNBs were founded to outperform in MB degradation the commercial P25 TiO_2 and the pristine TNBs under both UV and visible light. The result is believed to be caused by Au-induced Local Surface Plasmon Resonance (LSPR) effect. The size of Au particles, which is a critical factor in LSPR

effect, was adjusted by sintering temperature. It was shown that smaller particle size gave superior photocatalytic performance.

Table of Contents

List of Illustrations

List of Table

Chapter 1

INTRODUCTION

Titanium dioxide (TiO_2), or titania, is extensively used in photoelectrochemical reaction due to its chemical stability in harsh environment, non-toxicity and relatively low cost [1-2]. However, the large band gap of TiO_2, which is around 3.2eV, limits its absorption of sunlight only in the range of UV light; furthermore, 98% of the solar energy resides within the visible light region [2]. Different methods aimed at further improving photoactivity of TiO_2 within the visible spectra have been developed. Among them decorating metallic particles onto nanoscale titania is one of the most promising approaches. While utilizing the unique properties of nanoscale materials such as large surface area and quantum confinement effect [3], different decorated metals such as Pd [4], Ni [5] and Ag [6] have been reported to enhance the photocatalytic performance of TiO_2 within visible light range. Among the metals, Au is preferred due to its strong resistance to oxidation and corrosion [7].

The enhancement of photocatalytic performance of TiO_2 by Au decoration could be explained by the so-called local surface plasmon resonance (LSPR) effect, which is the coherent oscillation of free electrons in resonance with the electrical field component of the incoming electromagnetic irradiation for certain metallic nanostructures. LSPR effect is believed to greatly enhance the absorption of electromagnetic energy as well as the local optical field [3]. Enhancement of photocatalytic activity therefore can be observed for metal-decorated semiconductor materials such as Au-TiO_2.

In this thesis, Au-TiO_2 photocatalyst was obtained via a simple two-step soft chemical process. Hydrothermal synthesis, which is widely used to obtain ceramic powders, was used to synthesize anatase TiO_2 nanobelts (TNBs). Hydrothermal

synthesis has been proved to offer many advantages such as effectively excluding impurities, improved control of size and morphology, and low cost [8]. Continuous magnetic stirring was introduced during the synthesis aiming at modifying the morphology and improving photocatalytic performance of TNBs. It is found that this stirring-assisted hydrothermal synthesis can yield highly crystalline orientated one-dimensional TNBs with high aspect ratio. Au particles were subsequently decorated onto the obtained TNBs under room temperature. The size of the Au particles, which is a critical factor influencing the frequency of the surface plasmon absorption, was adjusted by post-heat treatment. Methylene Blue photodegradation, which has been widely studied and used to describe the photoactivity of photocatalysts [9-11], was employed to examine the photocatalytic performance and TNBs and Au-TNBs.

The thesis is organized into four chapters. Chapter one is a general introduction to Au-TNBs and the main focus of the research. Chapter two describes the background of our research including the photocatalytic mechanism of TiO_2, the improvement of photoactivity by LSPR effect, and the modification of hydrothermal synthesis by introducing magnetic stirring. The experimental part is summarized in Chapter three, starting with the detailed synthesis process of TNBs, characterization of obtained materials including SEM, XRD, UV-Vis, Raman and Methylene Blue degradation. Chapter three continues with the synthesis and characterization of Au-TNBs. The results are provided in Chapter four, which also includes the discussion as well as the final conclusion.

Chapter 2

BACKGROUND

2.1 Titanium Dioxide

It has been 33 years since Akira Fujishima and Kenchi Honda discovered the mechanism of photolysis of water using a TiO_2 electrode [1]. Since then, TiO_2 is extensively studied to become one of the most promising photocatalysts among all possible semiconductor materials. The photolysis process can be described in the following equation:

$$TiO_2 + 2h\nu \rightarrow 2p^+ + 2e^- \qquad \text{(e.q. 2.1.1)}$$

$$2p^+ + H_2O \rightarrow \frac{1}{2}O_2 + 2H^+ \qquad \text{(e.q. 2.1.2)}$$

$$2e^- + 2H^+ \rightarrow H_2 \qquad \text{(e.q. 2.1.3)}$$

The key process is the excitation of TiO_2 by light (e.q. 2.1.1) that create electrons and holes as free charge carriers. For anatase TiO_2, the band gap energy between valence band and conduction band is 3.2 eV, which means light of which wavelength shorter than 388 nm would be able to activate the electrons at the valence band. Activated electrons will jump to conduction band, leaving holes behind. The separated charge carriers are usually consumed by a recombination process, which is non-productive and significantly limits the efficiency of the photocatalytic reaction.

One of the most important advantage of TiO2 is its electrochemical stability in harsh environment. Common semiconductors such as silicon and gallium asenide could

be easily degraded under harsh environment [3], which greatly reduces their chances as photocatalysts since highly oxidative or highly reductive electrolyte is usually used in electrochemical reactions. TiO2, however, is extremely stable in acidic and basic solutions, offering a great advantage even the light harvest efficiency is lower. Other advantages TiO_2 can offer include its low cost and nontoxicity. TiO_2 is always considered environmental friendly and can also be used to purify water by reducing the concentration of organic pollutant [12]. TiO_2/UV photocatalytic degradation of typical dyes such as methylene blue, methyl red and congo red has been reported [9, 11]. The detailed mechanism of methylene blue degradation would be discussed further as it is the method used in the thesis to characterize the photocatalytic performance of our synthesized materials.

Methylene blue is a hetero-cyclic aromatic chemical compound with the molecular formation $C_{16}H_{18}N_3SCl$. It is reported that TiO_2 can degrade the dye upon the excitation of UV light, completely mineralizing carbon, nitrogen and sulfur into CO_2, NH_4^+, NO_3^- and SO_4^{2-}, respectively [9]. The detailed pathway is given in Fig. 2.1. The initial step that releases very active OH^o radicals is given (e.q. 2.2.1 to e.q. 2.2.5), and a multiple-step oxidation process is triggered as OH^o radicals continuously attack the functional groups in MB. The first step is the cleavage of the bonds of the $C\text{-}S^+\text{=}C$ functional group (e.q. 2.3.1), followed by a series of oxidation process that convert S and N into their maximum oxidation degree (e.q. 2.3.2 to e.q. 2.3.5, e.q 2.4.1 to e.q. 2.4.3).

$$(H_2O \Leftrightarrow H^+ + OH^-) + h^+ \rightarrow H^+ + OH^o \qquad \text{(e.q. 2.2.1)}$$

$$O_2(g) + e^- \rightarrow O_2^{o-} \qquad \text{(e.q. 2.2.2)}$$

$$O_2^{o-} + H^+ \rightarrow HO_2^{\ o} \quad \text{(e.q. 2.2.3)}$$

$$2HO_2^{\ o} \rightarrow H_2O_2 + O_2 \quad \text{(e.q. 2.2.4)}$$

$$H_2O_2 + e^- \rightarrow OH^- + OH^o \quad \text{(e.q. 2.2.5)}$$

$$R - S^+ = R' + OH^o \rightarrow R - S(=O) - R' + H^+ \quad \text{(e.q. 2.3.1)}$$

$$H^+ + e^- \rightarrow H^o \quad \text{(e.q. 2.3.2)}$$

$$NH_2 - C_6H_3R - S(=O) - C_6H_4 - R + OH^o \rightarrow NH_2 - C_6H_4 - R + SO_2 - C_6H_4 - R \quad \text{(e.q. 2.3.3)}$$

$$SO_2 - C_6H_4 - R + OH^o \rightarrow R - C_6H_4 - SO_3H \quad \text{(e.q. 2.3.4)}$$

$$R - C_6H_4 - SO_3H + OH^o \rightarrow R - C_6H_4^{\ o} + SO_4^{\ 2-} + 2H^+ \quad \text{(e.q. 2.3.5)}$$

$$R - C_6H_4 - NH_2 + OH^o \rightarrow R - C_6H_4 - OH + NH_2^{\ o} \quad \text{(e.q. 2.4.1)}$$

$$NH_2^{\ o} + H^o \rightarrow NH_3 \quad \text{(e.q. 2.4.2)}$$

$$NH_3 + H^+ \rightarrow NH_4^{\ +} \quad \text{(e.q. 2.4.3)}$$

$$R-C_6H_4-N(CH_3)_2+OH^o$$
$$\rightarrow R-C_6H_4-N(CH_3)-CH_2{}^o+H_2O \quad \text{(e.q. 2.5.1)}$$

$$R-C_6H_4-N(CH_3)-CH_2{}^o+OH^o$$
$$\rightarrow R-C_6H_4-N(CH_3)-CH_2OH \quad \text{(e.q. 2.5.2)}$$

$$R-C_6H_4-N(CH_3)-CH_2OH+OH^o$$
$$\rightarrow R-C_6H_4-N(CH_3)-CH^o-OH+H_2O \quad \text{(e.q. 2.5.3)}$$

$$R-C_6H_4-N(CH_3)-CH^o-OH+OH^o$$
$$\rightarrow R-C_6H_4-N(CH_3)-CH(OH)_2$$
$$\rightarrow R-C_6H_4-N(CH_3)-CHO+H_2O \quad \text{(e.q. 2.5.4)}$$

$$R-C_6H_4-N(CH_3)-CHO+OH^o$$
$$\rightarrow R-C_6H_4-N(CH_3)-C^o=O+H_2O \quad \text{(e.q. 2.5.5)}$$

$$R-C_6H_4-N(CH_3)-C^o=O+OH^o$$
$$\rightarrow R-C_6H_4-N(CH_3)-COOH \quad \text{(e.q. 2.5.6)}$$

$$R-C_6H_4-N(CH_3)-COOH+h^+$$
$$\rightarrow R-C_6H_4-N^o-CH_3+CO_2(g)+H^+ \quad \text{(e.q. 2.5.7)}$$

The degradation rate depends highly on the electron-hole generation rate in TiO_2. Comparison between the photoactivity of different TiO_2 samples can be made by measuring the degradation rate, i.e. the concentration reduction rate of MB.

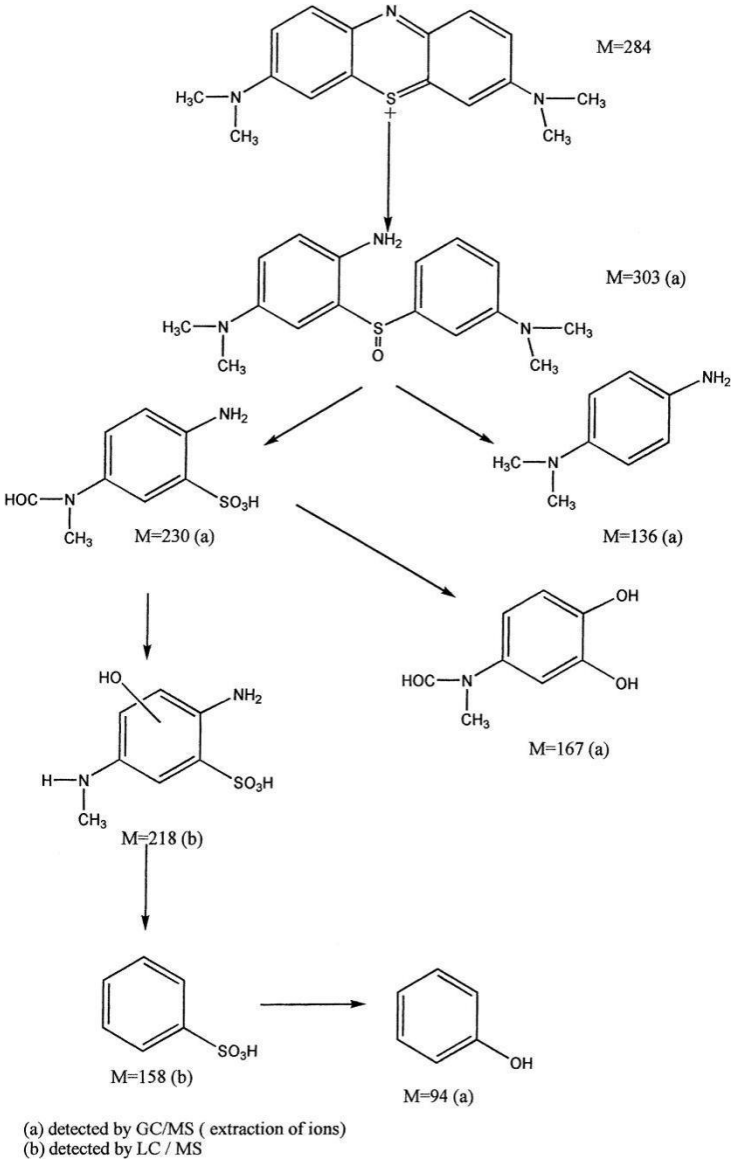

Fig. 2.1 Degradation pathway of MB

One of the significant drawbacks that limits the potential application of TiO_2 photocatalyst is the large band gap between the conduction band and the valence band. To generate free charge carriers, the energy of inciting light must overcome the band gap energy, which for anatase TiO_2 is 3.2 eV. Even though it is smaller to that of some

semiconductors such as ZnO (3.35 eV) and SnO_2 (3.6 eV), it is not enough to harvest most of the energy in visible light (400 nm to 700 nm). In other words, TiO_2 has significantly low photocatalytic efficiency under visible light, compared to GaAs and Si [3]. However, both of them are prone to degradation in harsh environment as discussed above. Challenges remain on developing a photocatalyst that is both efficient and stable during photoelectrochemical reactions.

2.2 Hydrothermal Synthesis

Hydrothermal synthesis is defined as a process that utilizes single or heterogeneous phase reactions in aqueous media at elevated temperature (T>25 ^oC) and pressure (P>100 kPa). The research started as early as 19th century as geologists tried to simulate natural hydrothermal phenomena. It was recognized as an important method to grow single crystal in the 20th century. However, the critical reaction conditions limited the commercialization. It was not until recent years that people's interest rose again as more and more ceramic powders were proved to be able to be obtained under mild conditions (T<350 ^oC, P<100 MPa) [8]. The moderate reaction conditions offer a significant advantage as reactors that must sustain the pressure and the temperature during the reaction would be much cheaper.

Hydrothermal synthesis offers many other advantages. First of all, nearly all forms of ceramics can be obtained via hydrothermal synthesis. When considering the production of ceramic powders, it costs far less time and energy because high-temperature calcination, mixing and milling are either unnecessary or minimized. Size and morphology control are superior than other methods since the rate of nucleation and growth are relatively uniform. Particles with desired shape and crystallographic directions can be synthesized such as plates, cubes, tubes, wires and rods. Another advantage is

the excessive purity of the synthesized materials over the starting materials. Hydrothermal synthesis is considered as a self-purifying process as materials will reject the presence of impurities during the growth process. Hydrothermal synthesis can take place in a variety of aqueous systems. Compared to solid phase process, it takes shorter time for diffusion, absorption, nucleation and crystallization. Last but not the least, hydrothermal synthesis offers opportunities for continuous mass production.

A variety of materials can be obtained via hydrothermal synthesis. Among them most common are oxide ceramic materials. Simple oxide such as ZrO_2, TiO_2, ZnO, Fe_2O_3, SnO_2, Co_3O_4, etc., are reported to be synthesized. Complex oxide like $BaTiO_3$, $PbTiO_3$, $KNbO_3$, etc., can also be obtained. Final products can be in a variety of forms such as cubes, spherical, fibers, plates, nanorods, nanobelts, nanotubes, etc.

In hydrothermal synthesis, variable thermodynamic parameters are proven to be related to the size and morphology of the final product. Among them concentrations of reactants, pH and temperature are the most important. Table 2.1 summarizes some experimental results in TiO_2 hydrothermal synthesis that have been reported in literature. Some non-thermodynamic parameters, however, also have impact on the size and morphology of the product. In the thesis, the impact of stirring speed during TiO_2 synthesis is discovered and studied, which would be discussed furthermore.

Table 2.1 TiO_2 product under different hydrothermal conditions starting with various precursors [14-16]

Starting Materials	Hydrothermal Conditions	Product
Anatase/rutile/P25 TiO_2 + 10-15 M NaOH	100-150 ^oC 24-48 hrs	Hybrid rutile/anatase nanotubes
Crystalline/amorphous TiO_2 + 5-15 M NaOH	180-250 ^oC 24-48 hrs	Hybrid rutile/anatase nanoribbons
Rutile TiO_2 + 10 M NaOH	100-150 ^oC 48 hrs	Rutile nanotubes
Rutile TiO_2 + 10 M NaOH	170-180 ^oC 30 hrs	Rutile nanorods
Anatase TiO_2 + 10 M NaOH	180 ^oC 48 hrs	Anatase nanobelts

Growth Mechanisms of these 1D TiO_2 nanostructures were studied and they differs from each other when different hydrothermal conditions are applied. Nevertheless, it is believed that high concentration NaOH breaks the original Ti-O-Ti bonds and promotes anisotropic growth [13]. In the case of TNBs in this study, the growth along [010] direction is accelerated. The chemical process is given in e.q. 2.6.1 to e.q. 2.6.3. After the

acid washing, Na^+ are replaced by H^+, which are then removed during the subsequent high-temperature dehydration and crystallization process.

$$3TiO_2 + 2NaOH \rightarrow Na_2Ti_3O_7 + H_2O \quad \text{(e.q. 2.6.1)}$$

$$Na_2Ti_3O_7 + 2H^+ \rightarrow H_2Ti_3O_7 + 2Na^+ \quad \text{(e.q. 2.6.2)}$$

$$H_2Ti_3O_7 \rightarrow 3TiO_2 + H_2O \quad \text{(e.q. 2.6.3)}$$

2.3 Local Surface Plasmon Resonance Effect and Au-TiO_2 Photocatalyst

As discussed above, pure TiO_2 photocatalyst is not able to absorb the visible light effectively and It is very challenging to find a photocatalyst that meets both the requirement of efficiency and stability. One potential solution is the heterogeneous photocatalyst that combines the advantage of two or three materials. Usually, heterogeneous photocatalysts can offer three benefits [3]. First, light absorption could be enhanced as materials with small band gap can be used to sensitize semiconductors with large band gap. Second, the charge separation and transport could be more efficient as a p-n junction (semiconductor/semiconductor) or Schottky junction (metal/semiconductor) is created to generate a built-in electrical potential to separate electrons and holes more effectively. Co-catalyst effect is also a factor that enhances the photoactivity. Finally, sometimes heterogeneous photocatalysts are more stable than pure semiconductors.

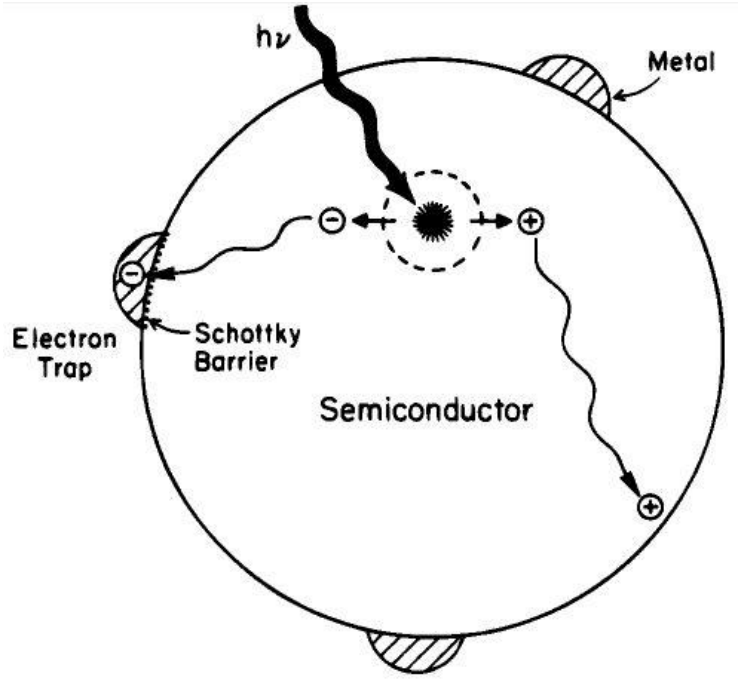

Fig. 2.2 Enhanced charge separation induced by Schottky barriers in metal-loaded semiconductor photocatalyst [17]

Among the well-studied heterogeneous photocatalysts, most of them are metal-loaded semiconductors: Au [2], Ag [6], Pt [18] and Pd [4] nanoclusters have been widely investigated. Ag-TiO_2 is such a typical photocatalyst, where Ag successfully creates a Schottky barrier between the two materials. While electrons migrate from TiO_2 to the surface of the Ag, the barrier prevents the recombination process. The separated holes then will diffuse to the surface of TiO_2 and participate in oxidizing organic dyes as discussed earlier. This would significantly increase the light harvest efficiency of TiO_2 [3]. Au in a similar way has been reported to increase the photoactivity not only in UV range, but also in visible light range. As shown in Fig. 2.3, under UV light the excited electrons

migrate to Au surface to involve in hydrogen evolution. Under visible light, photocatalytic reaction becomes totally different. While in TiO2 electrons in the valence band cannot be excited, free electrons from Au due to the LSPR effect are injected to the conduction band of TiO2, leaving holes in Au. Upon diffusing to the surface, they both act as reaction sites. The excited electrons in Au are a result of a coherent oscillation in resonance with the electrical field component of the incoming electromagnetic irradiation. The oscillation greatly enhances the absorption and photocatalytic performance of TiO_2 [3]. In this thesis, studies were carried out to understand the effect of size and shape of the loaded Au on the performance of Au-TiO_2.

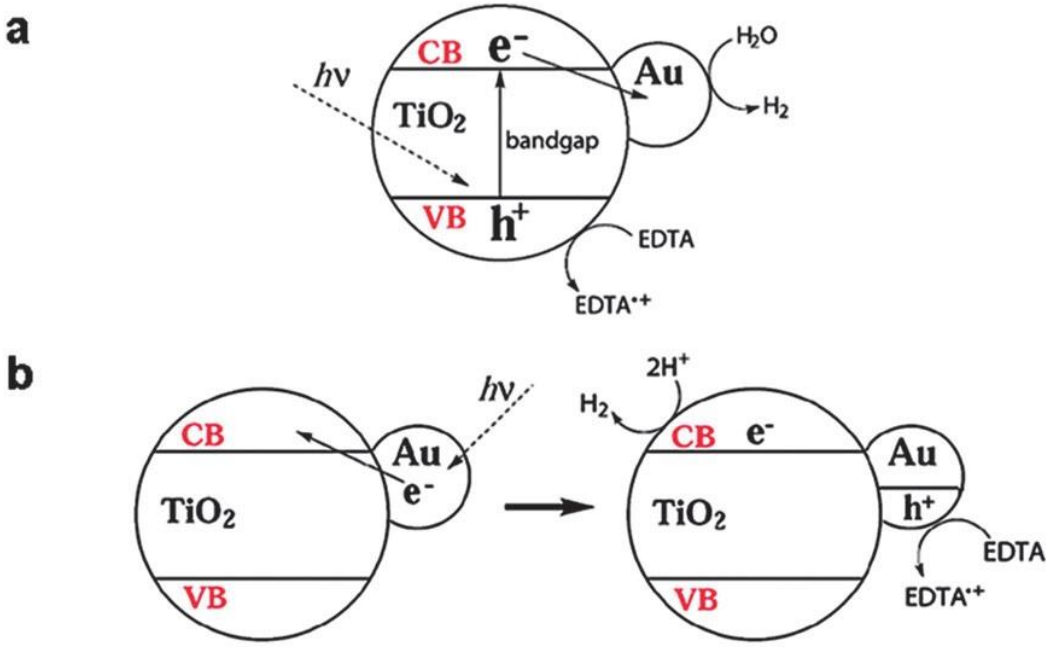

Fig. 2.3 The mechanism of photoactivity enhancement of Au-TiO_2 (a) under UV light and (b) under visible light [3]

In conclusion, hydrothermal synthesis offers a cost-effective method to synthesize highly active 1D anatase TiO_2 nanobelts i.e. TNBs, when combined with LSPR effect induced

by Au nanoparticles, giving us a photocatalyst performing superior to P25 TiO_2 in both UV range and visible light range. Simple ways to tune size and morphology of the photocatalyst were found, and how modification would influence the photoactivity was studied, which would be explained in details in the following chapters.

Chapter 3

EXPERIMENT

In this chapter, detailed experimental set-up is explained, which is divided into two parts: (1) the stirring-assisted hydrothermal synthesis of TiO_2 nanobelts (TNBs) and the synthesis of Au-TNB heterogeneous photocatalyst; (2) The characterization of the obtained materials, including the methylene blue degradation test.

3.1 The synthesis of TNB and Au-TNB

The stirring-assisted hydrothermal synthesis is modified from Wang et al [16] to obtain TNBs. 1.2 g anatase TiO_2 powder (Alfa Aesar, 99.7%, 15 nm APS powder) was mixed with 80 ml of 10 M NaOH solution. After that, 25 ml of the mixture was transferred to a Teflon-lined stainless steel reactor and heated up to 200 ^oC by a band heater. Temperature was continuously monitored by a thermal couple attached to the band heater and a relay was used to maintain the desired temperature. The reactor was placed on a hotplate (Fisher Scientific) so that with a small magnetic stir bar inside the Teflon chamber, the magnetic stirrer can provide the desired stirring. The rotation speed was set at 0 rpm (no stirring), 100 rpm, 250 rpm, 500 rpm and 700 rpm, respectively. After 48 hours, the obtained product was filtered and washed with 0.06 M HCl solution and deionized water until pH is neutral. The obtained product was dried in an oven at 80 ^oC for 2 hours. Post heat treatment was applied in order to obtain high crystallinity. The dried product was heated up to 700 ^oC in a tube furnace at the rate of 1 ^oC/min for 30 min and cooled down at the rate of 10 ^oC/min. White and flurry powder was obtained as our final product.

To obtain Au-TNBs, 0.1 g TNBs (rotation speed is set at 250 rpm) were added to 16.7 ml deionized water. 0.5 ml 0.01 M $HAuCl_4$ was mixed with them in an equivalent amount to 1.0 wt% of Au. To form Au nanoparticles, 0.43 ml of 0.01 M $NaBH_4$ solution was added under vigorous stirring for 20 min. After that, the obtained Au-TNBs were carefully washed by deionized water. By using this chemical method, the loaded Au particles can be as small as 5 nm. Au-TNBs with larger Au particle size can be obtained via post heat-treatment. The product was heated up in a tube furnace up to 400 ^oC at the rate of 1 ^oC/min for 4 hours. A schematic illustration of the experimental set-up is given in Fig. 3.1.

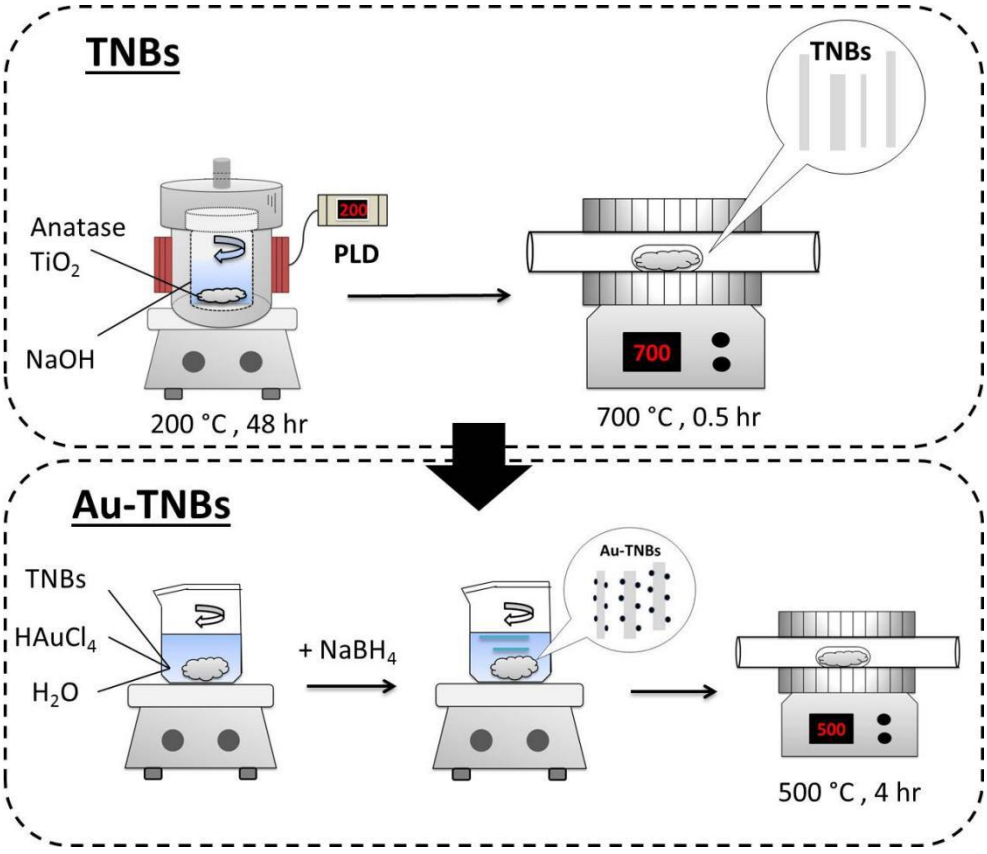

Fig. 3.1 Experimental set-up of synthesizing TNBs and Au-TNBs

3.2 The Characterization and Photoactivity Test

The morphology of the obtained product was observed with high-resolution field emission scanning electron microscope (FE-SEM, Hitachi S4800). The crystal structure was identified by X-ray diffraction (XRD, D-500). UV-Vis spectra that were used to characterize the optical property of the samples was obtained by a Perkin-Elemer Lambda 35 spectrometer. Raman spectra was obtained by a Raman spectrometer (Thermo Scientific DXR). X-ray photoelectron spectroscopy (XPS, Perkin-Elmer Phi 560 XPS/Auger system) was used to characterize the chemical state information from the surface. Brunauer-Emmett-Teller (BET) surface area is measured by Sid Richardson Carbon & Energy Company.

MB degradation rate is used as a standard for the photoactivity of our photocatalysts. A portable UV lamp (4W) at 360nm was used as a UV irradiation source. A Xenon arc lamp (500W) with 455 nm long pass filter was chosen to be the visible light source. 3 mg TNBs/Au-TNBs were added in 10 ml methylene blue solution, the mixture was stirred at 700 rpm in a quartz beaker while be irradiated at a distance of 15 cm in a dark chamber. After that, the mixture was taken out, centrifuged to separate all solid materials from the solution, and analyzed by UV-Vis spectrometer. The characteristic absorption peak of MB is around 663 nm.

Chapter 4

RESULTS AND DISCUSSION

4.1 Characterization of TNBs with Different Rotation Speed

4.1.1 SEM images

TNBs obtained via stirring-assisted hydrothermal synthesis was observed under FE-SEM. To study the impact of rotation speed on the morphology, a total of ten samples were obtained. Table 4.1 summarizes the difference between each sample.

Table 4.1 SEM sample numbers, their corresponding conditions and figure numbers

Sample number	Condition	Figure number
A1	0 rpm no heat treatment applied	Fig. 4.1
A2	0 rpm Heat treatment applied	Fig. 4.2
B1	100 rpm No heat treatment applied	Fig. 4.3
B2	100 rpm Heat treatment applied	Fig. 4.4

Table 4.1 - continued

C1	250 rpm No heat treatment applied	Fig. 4.5
C2	250 rpm Heat treatment applied	Fig. 4.6
D1	500 rpm No heat treatment applied	Fig. 4.7
D2	500 rpm Heat treatment applied	Fig. 4.8
E1	700 rpm No heat treatment applied	Fig.4.9
E2	700 rpm Heat treatment applied	Fig. 4.10

In both Fig. 4.1 and 4.2, clear belt shape was observed. The aspect ratio varies from each other. The small and broken belts and the zigzag edge of the TNBs in Fig. 4.2 indicate that during the high-temperature crystallization process shrinkage of volume could create structural changes of the TNBs. The breaking happened along certain crystallographic planes as hydrogen and oxygen atoms were removed. In Fig. 4.3 and

4.4, with the increase of stirring speed (100 rpm), nanobelts start to extend in length, resulting higher aspect ratio. Same flaking belts are observed in Fig. 4.4. When rotation speed increases to 250 rpm, more slender belts were observed (Fig. 4.5 and 4.6). Same trend applies when rotation speed continuously increases to 500 rpm and 700 rpm (Fig 4.7 to 4.10). From all these SEM images, a conclusion can be drawn that rotation speed has a consistent impact on the aspect ratio of TNBs: stirring can promote the anisotropic growth of TNBs, possibly through the internal shear force induced. By simply adjusting the rotation speed, the size and morphology of TNBs can be tuned.

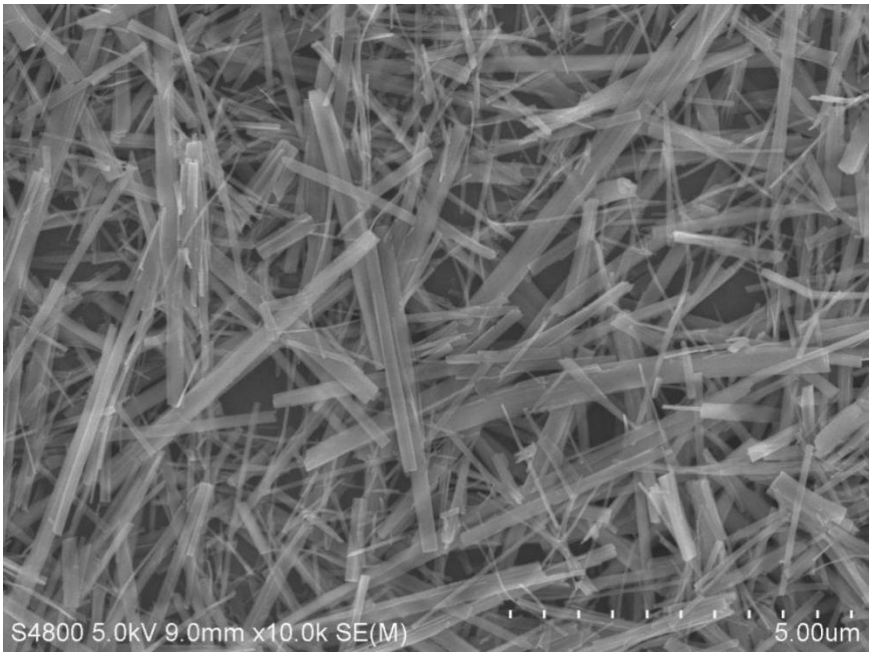

Fig. 4.1 Sample A1 (0 rpm, no heat treatment)

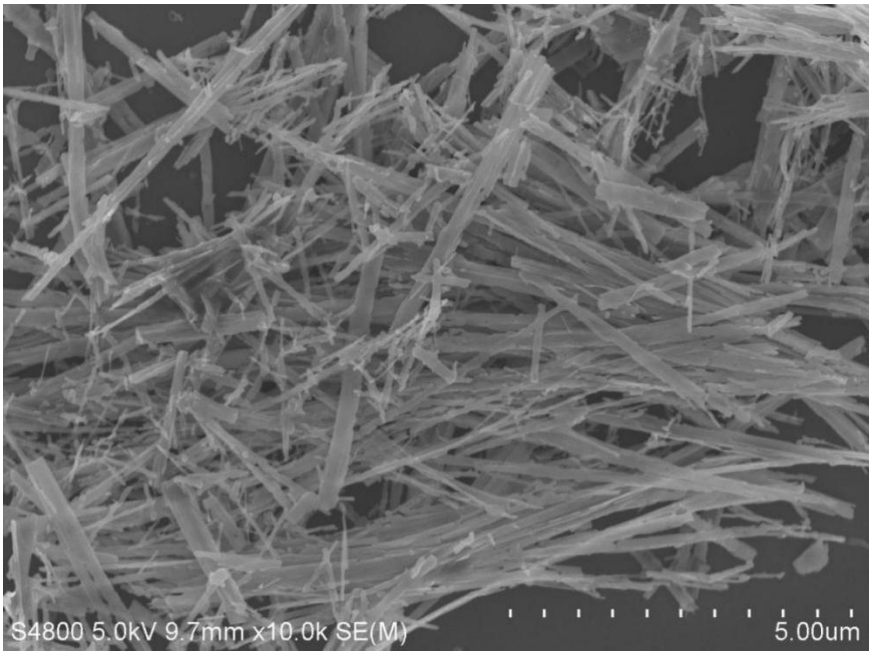

Fig. 4.2 Sample A2 (0 rpm, heat treatment)

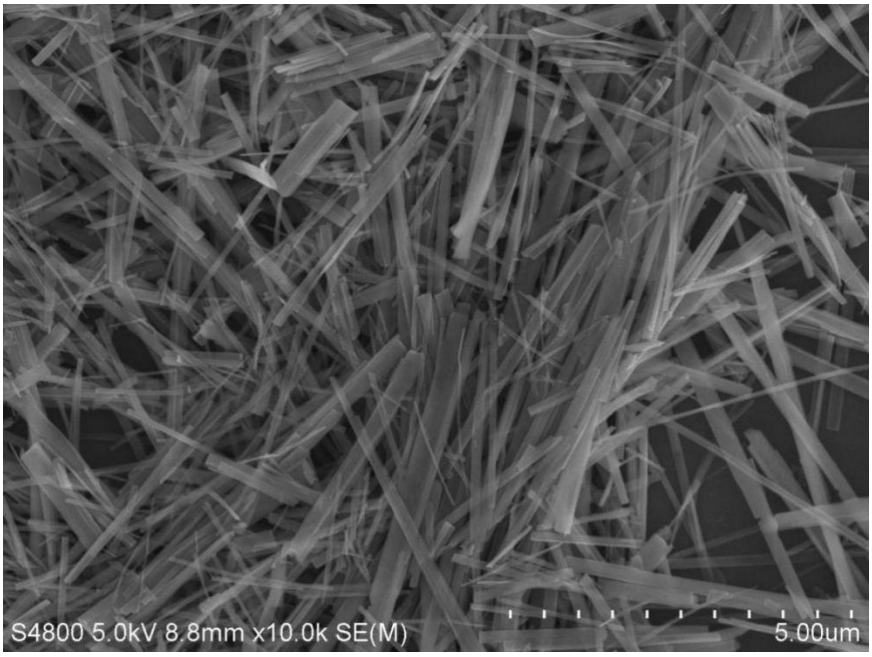

Fig. 4.3 Sample B1 (100 rpm, no heat treatment)

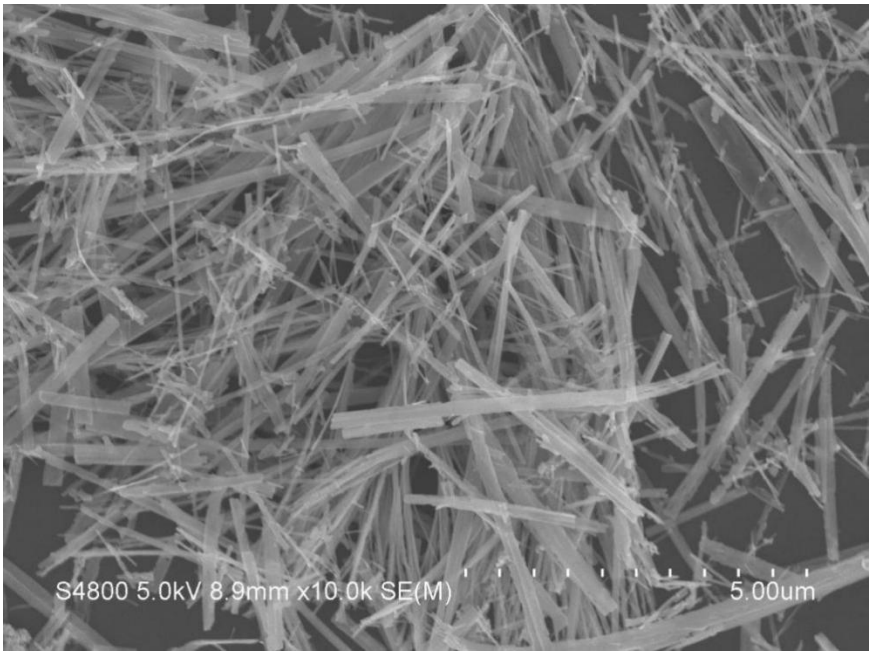

Fig. 4.4 Sample B2 (100 rpm, heat treatment)

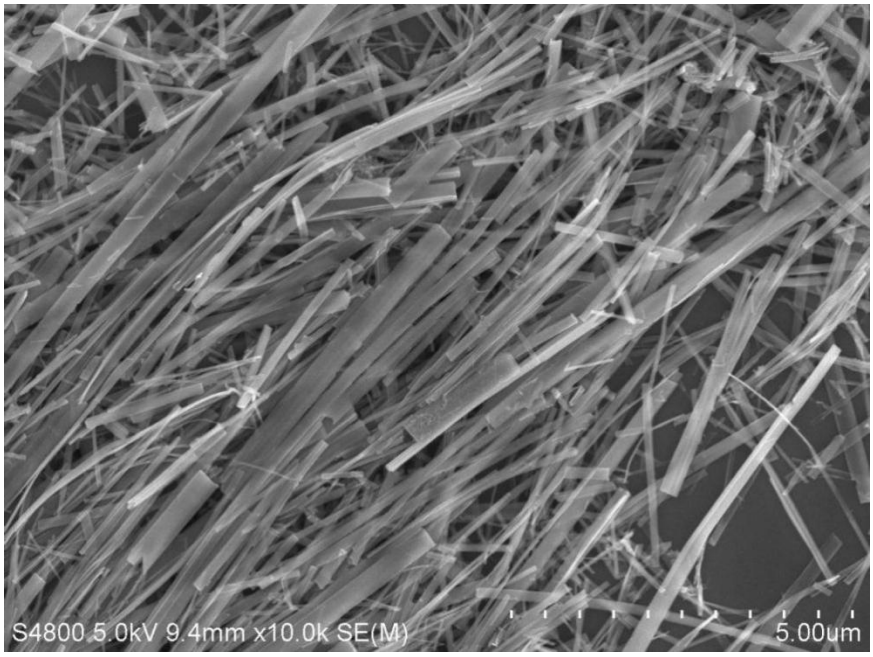

Fig. 4.5 Sample C1 (250 rpm, no heat treatment)

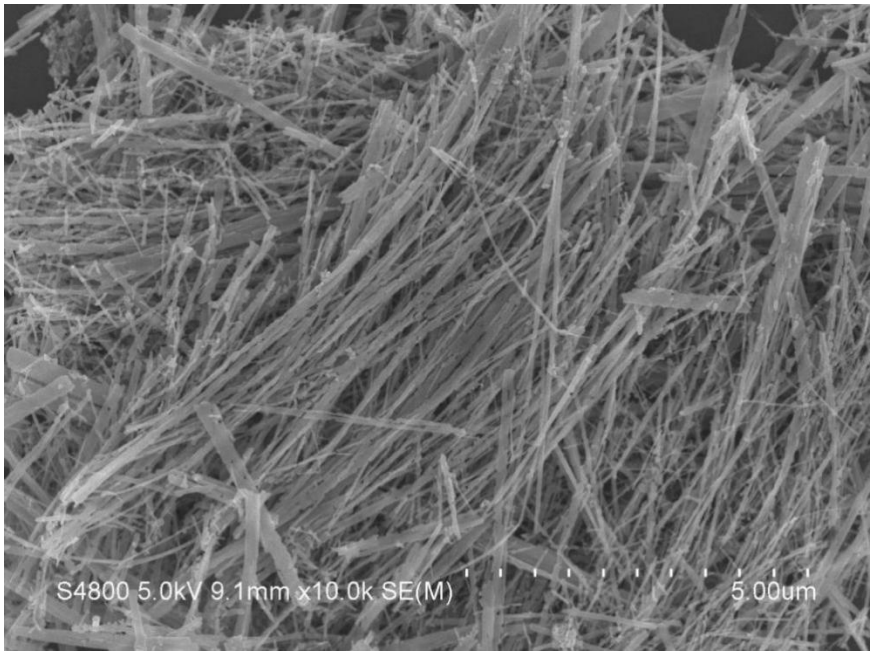

Fig. 4.6 Sample C2 (250 rpm, heat treatment)

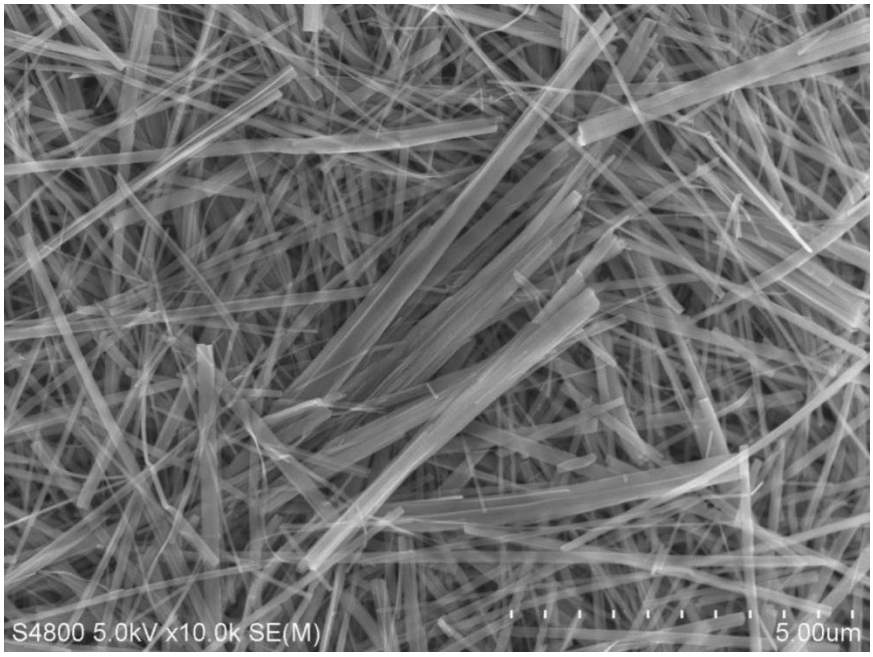

Fig. 4.7 Sample D1 (500 rpm, no heat treatment)

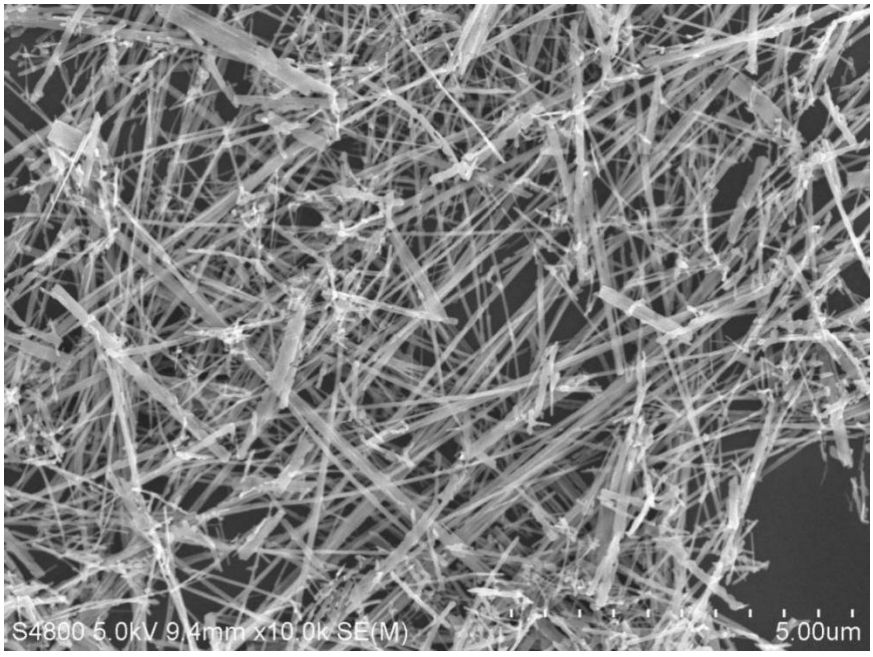

Fig. 4.8 Sample D2 (500 rpm, heat treatment)

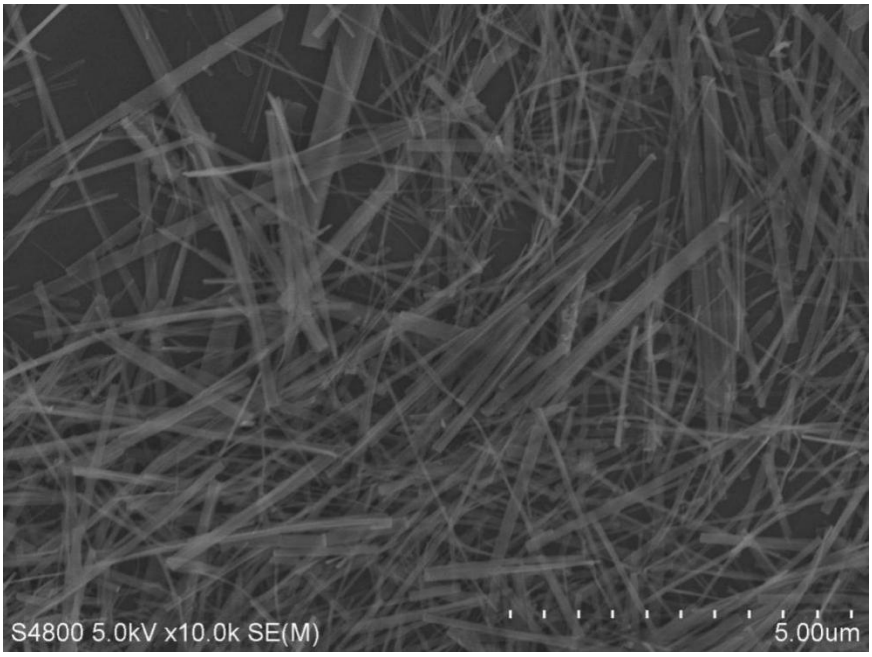

Fig. 4.9 Sample E1 (700 rpm, no heat treatment)

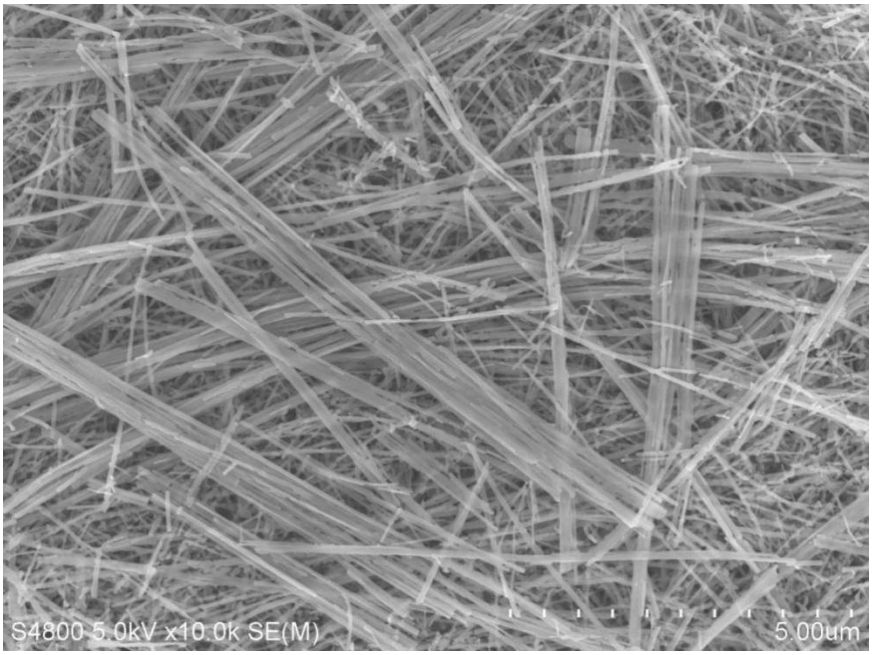

Fig. 4.10 Sample E2 (700 rpm, heat treatment)

4.1.2 XRD pattern

Apart from that, rotation speed seems not to have any influence on the crystallinity of TNBs, as revealed by the XRD results of calcined samples (A2, B2, C2, D2, and E2) in Fig.4.11. According to JCPDS card No. 21-1272, all peaks in the XRD scan range could be identified as anatase TiO_2. The characteristic crystallographic plane of anatase phase is marked in the graph. No other peaks could be found, ensuring the high purity of TNBs. Peak intensity is high compared to background noise, indicating very good crystallinity for a powder sample.

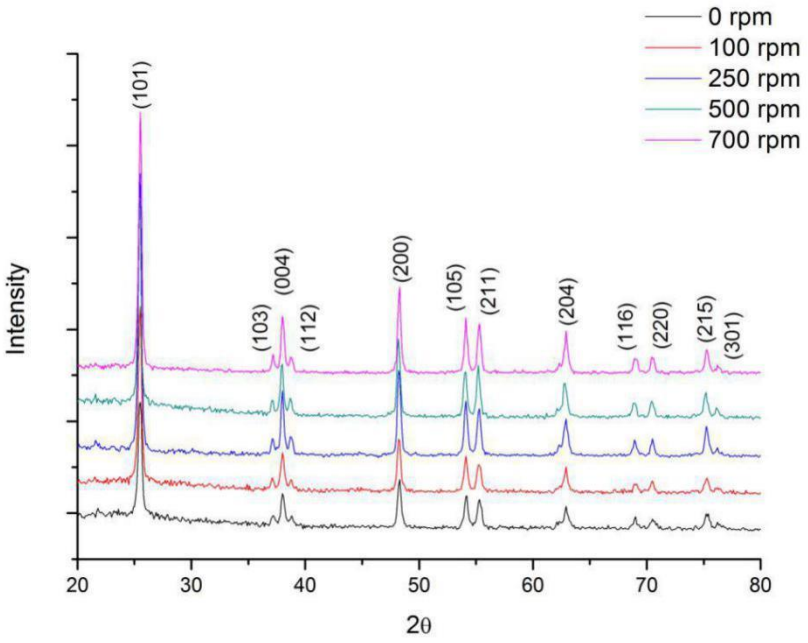

Fig. 4.11 XRD patterns of all calcined TNBs

4.1.3 Raman spectra

On the basis of factor group analysis, Anatase TiO_2, which is a tetragonal crystal, has six active Raman modes ($3E_g + 2B_{1g} + 1A_{1g}$) [19]. E_g mode is the symmetrical stretching vibration of O-Ti-O bond in TiO_2, while A_{1g} mode is the asymmetrical bending vibration of O-Ti-O and B_{1g} mode is the symmetrical bending vibration of O-Ti-O. In the Raman spectra (Fig. 4.12), the following Raman modes are observed: three E_g modes at 144, 197 and 649 cm^{-1}, and two B_{1g} modes at 399 and 519 cm^{-1}. One of the B_{1g} mode is overlapped with one A_{1g} mode (514 cm^{-1}). It clearly reveals that as rotation speed increases, no phase transformation happens as there are no peak shifts. No rutile or brookite phase is observed. Highly crystallized anatase phase remains stable despite the stirring.

Relative intensity ratio between A_{1g} mode at 514 cm^{-1} and E_g mode at 144 cm^{-1} was calculated according to the original data. The results are summarized in Table 4.2. An obvious trend shows that as rotation speed increases, the intensity ratio also increases. According to Tian et al [21], this trend may reveals an increased percentage of exposed (001) facets in the TNBs: As shown in Fig. 4.13., anatase TiO_2 (101) surface, which is the most thermodynamically stable surface, consists saturated 6c-Ti and 3c-O bonding modes together with 5c-Ti and 2c-O unsaturated bonding modes. However, anatase TiO_2 (001) surface consists of unsaturated 5c-Ti and 2c-O bonding modes only, possibly explaining its higher surface energy. This difference in surface structure may be the reason for the relative intensity change in Raman spectra. When exposed (001) facets exist, the number of symmetrical stretching vibration mode decreases, and the number of asymmetrical bending mode increases, thus the relative intensity ratio between A_{1g} and E_g modes increases. Since there is no experimental condition change

except for the rotation speed, a conclusion can be made that TNBs have higher aspect ratio when higher rotation speed is applied, and this change in morphology somehow leads to higher percentage of exposed (001) facets among the whole surface area. How this change in surface structure influences the photoactivity of TNBs is discussed in Section 4.1.5.

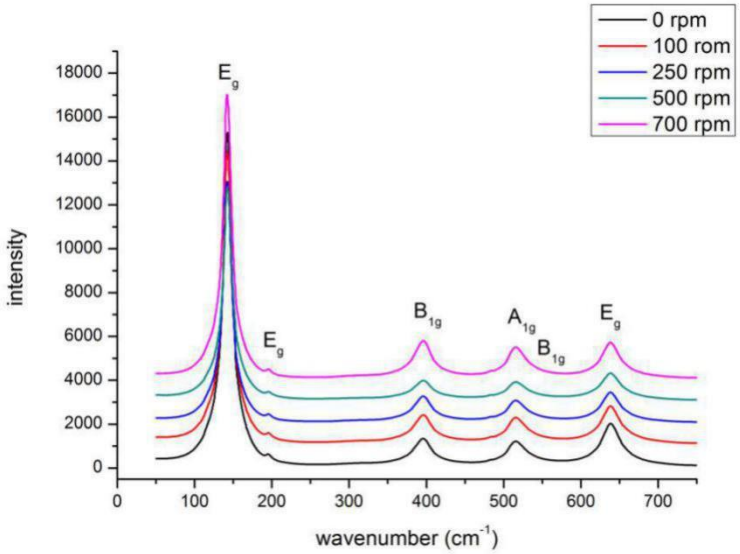

Fig. 4.12 Raman spectra of all calcined TNBs

Table 4.2 Relative intensity ratio between A_{1g} mode and E_g mode of all TNBs

Rotation speed (rpm)	0	100	250	500	700
I_{A1g}/I_{Eg} (a.u.)	0.0840	0.1680	0.2505	0.3175	0.3537

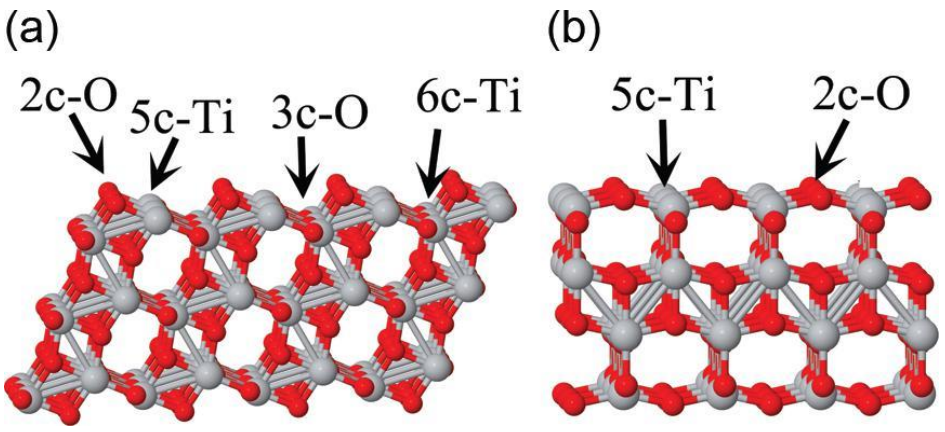

Fig. 4.13 Structure models of anatase TiO_2: (a) (101) surface and (b) (001) surface [21]

4.1.4 UV-Vis spectra

UV-Vis absorption spectra show that the obtained TNBs have good response to the inciting UV light which is independent on the applied rotation speed; absorbance is high when wavelength is shorter than 380 nm and drops significantly after that. Rotation speed does not have impact on the UV-Vis spectra though the TNBs created at different rotation speeds vary in aspect ratio.

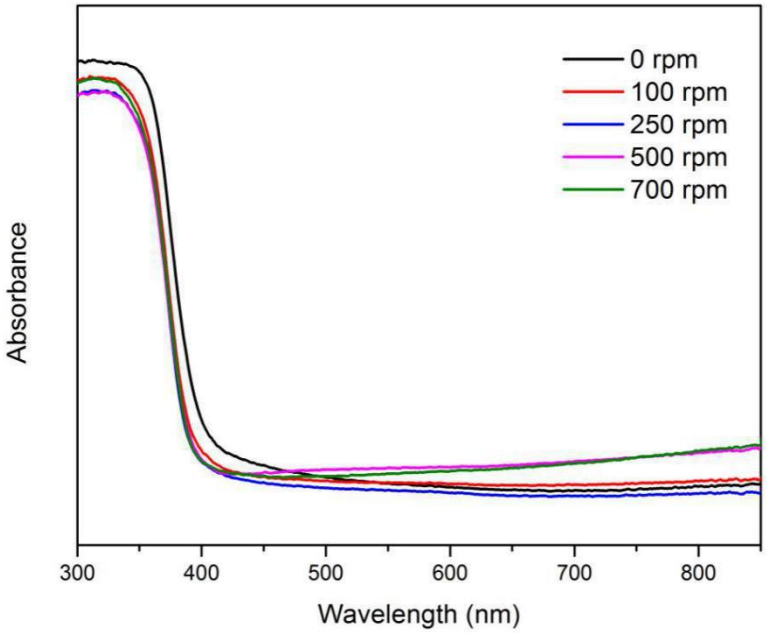

Fig. 4.14 UV-Vis spectra of all calcined TNBs

4.1.5 MB degradation curves & specific degradation rate

In order to study the impact of rotation speed on the photoactivity, photodegradation curve of MB showing $\ln(C/C_0)$, where C and C_0 are the MB concentration before and after degradation, as a function of degradation time t under UV light illumination is plot in Fig. 4.15.

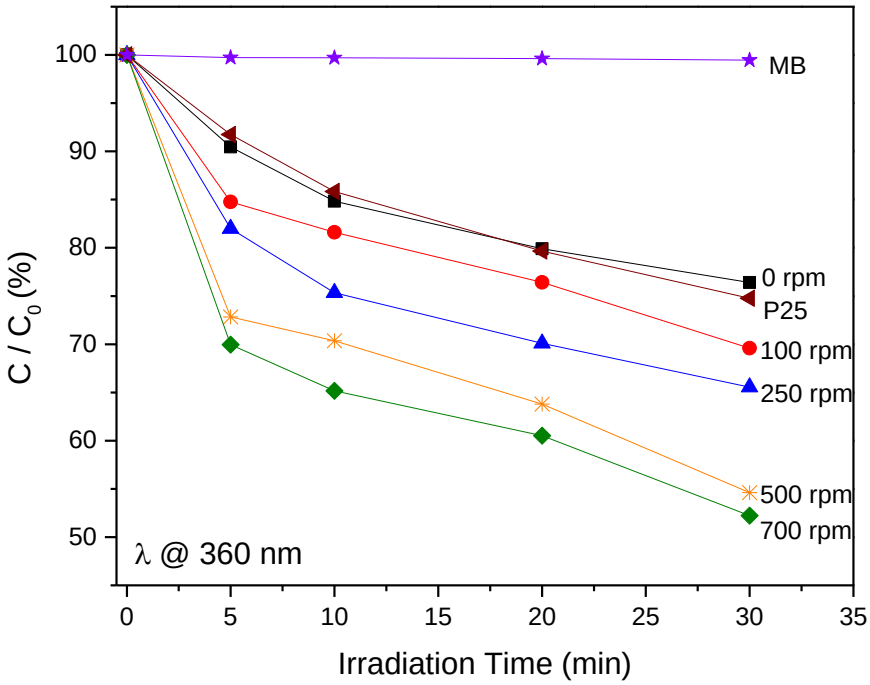

Fig. 4.15 MB degradation curves of P25 and all TNBs

The photodegradation process lasted for 30 min. The consistent increase in degradation rate with the increase of rotation speed was observed. The concentration of MB drops more significantly in the first 5 min, and the degradation rate becomes smaller after that. P25 and 0-rpm-TNBs shows the worst photocatalytic performance as the concentration of MB is more than 75% of C_0 after 30 min. As rotation speed increases, TNBs show improved photoactivity. 100-rpm-TNBs already have better degradation performance than both 0-rpm-TNBs and P25. The trend remains as the concentration of MB drops to nearly 52% after 30 min of illumination for 700-rpm-TNBs. Therefore conclusion can be made that there is a consistent relationship between rotation speed and photoactivity from the results: higher rotation speed lead to better photoactivity,

which is possibly related to the higher aspect ratio of TNBs when we consider the morphology.

To step further in our study, The overall degradation results were taken to calculate the degradation rate of TNBs with different rotation speed respectively based on e.q. 4.1 [20], where t (min) is the photodegradation time and k (min^{-1}) is the first-order rate constant.

$$\ln(\frac{C_0}{C}) = kt \qquad \text{(e.q. 4.1)}$$

The results are summarized in Table 4.3.

Nanomaterials usually perform better than bulk materials by taking advantage of the high specific surface area. In the case of semiconductors, charge carriers have shorter diffusion length and more active sites when specific surface area is higher. To compare the surface area difference between our TNBs with different rotation speed, BET surface area measurement was carried out. The results are also summarized in Table 4.3. Surprisingly, 700-rpm-TNBs, which give us the best photocatalytic performance, turn out to have the lowest specific surface area. Consistent trend reveals that as rotation speed increases, TNBs become longer and narrower, and specific surface area shrinks. Specific degradation rate constant k' ($g*min^{-1}*m^{-2}$) was calculated respectively according to e.q. 4.2, where S_A is the measured specific surface area.

$$k' = \frac{k}{S_A} \qquad \text{(e.q. 4.2)}$$

Results are summarized in Table 4.3. Since 700-rpm-TNBs combine both the best photoactivity and the lowest specific surface area, the specific rate constant is significantly higher than others: nearly three times higher than 0-rpm-TNBs.

Table 4.3 degradation rate constant, specific surface area and specific degradation rate constant of TNBs with different rotation speed

Rotation speed (rpm)	0	100	250	500	700
k (min^{-1})	0.593×10^{-2}	0.697×10^{-2}	0.786×10^{-2}	1.056×10^{-2}	1.067×10^{-2}
S_A (m^2*g^{-1})	30.8820	26.3362	24.0008	22.2034	19.0269
k' ($g*m^{-2}*min^{-1}$)	1.920×10^{-4}	2.647×10^{-4}	3.275×10^{-4}	4.756×10^{-4}	5.608×10^{-4}

One possible explanation is that more active (001) facets are exposed when rotation speed is increased as discussed in section 4.1.3. Anatase TiO_2 has been reported to be more sensitive to inciting light on (001) facets other than (101) facets [22]. It is completely possible that even though specific surface area shrinks after rotation speed increases, the exposed (001) facets do not shrink as much, occupying more surface area of TNBs. Since TNBs are in pure anatase phase, higher percentage of exposed (001) facets results in better photocatalytic performance, leading to a higher specific degradation rate.

4.2 The characterization of Au-TNBs

4.2.1 XRD pattern

XRD scanning curves of Au-TNBs and normal TNBs are given in Fig. 4.16. Other peaks aside from anatase TiO_2 can be found, which can all be identified as Au according to JCPDS card No. 84-1286. The main peak Au (111) overlaps with anatase TiO_2 at around 38.2° and twists the original peak shape, followed by Au (200) at 44.4°, Au (220) at 64.5° and Au (311) at 77.5°. Au's peak intensity relatively lower, due to the low weight ratio of Au.

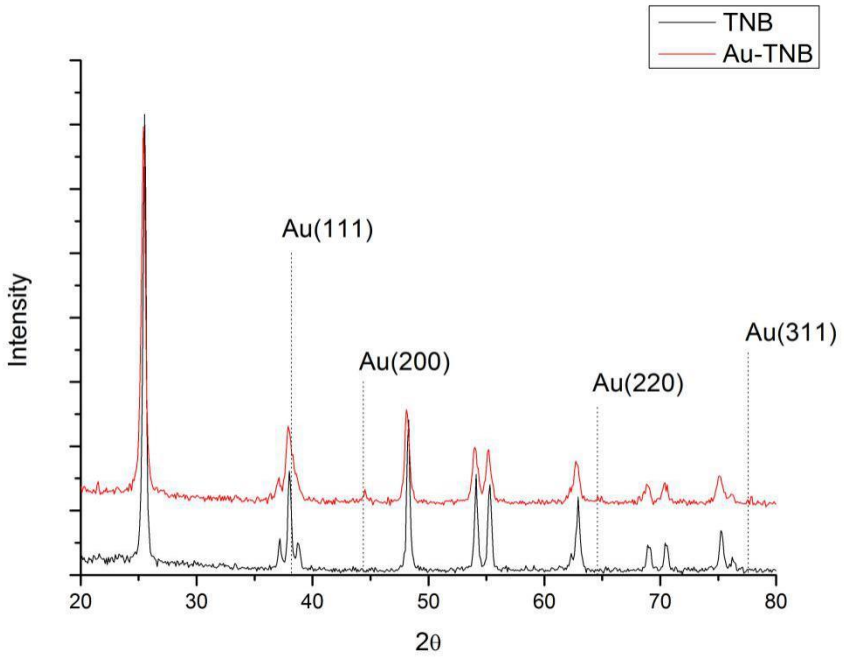

Fig. 4.16 XRD patterns of TNBs and Au-TNBs

4.2.2 HR-TEM images

HR-TEM images (Fig. 4.17 to 4.20) were taken to get better understanding on the morphology of Au-TNBs. The dark spherical structures in the images are Au particles, The TNBs reveal highly oriented crystallographic structure. Most part of the surface is still exposed as Au forms nanoparticles, occupying remaining part. The diameter of Au nanoparticles is around 4.6 nm for uncalcined Au-TNBs (designated as Au-TNB@RT) and 10 nm for calcined Au-TNBs (designated as Au-TNB@500C).

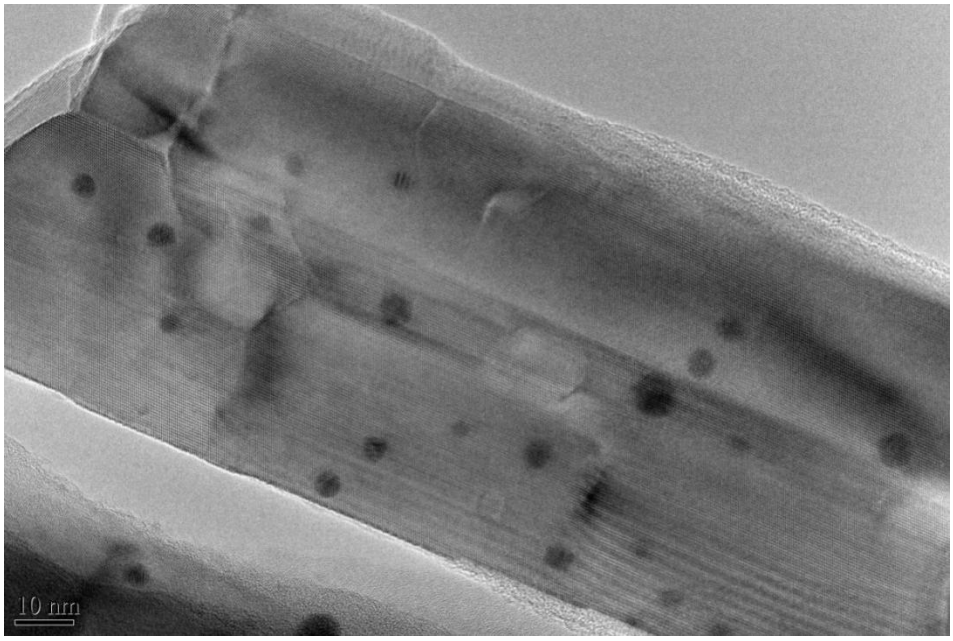

Fig. 4.17 HR-TEM image of Au-TNB@RT

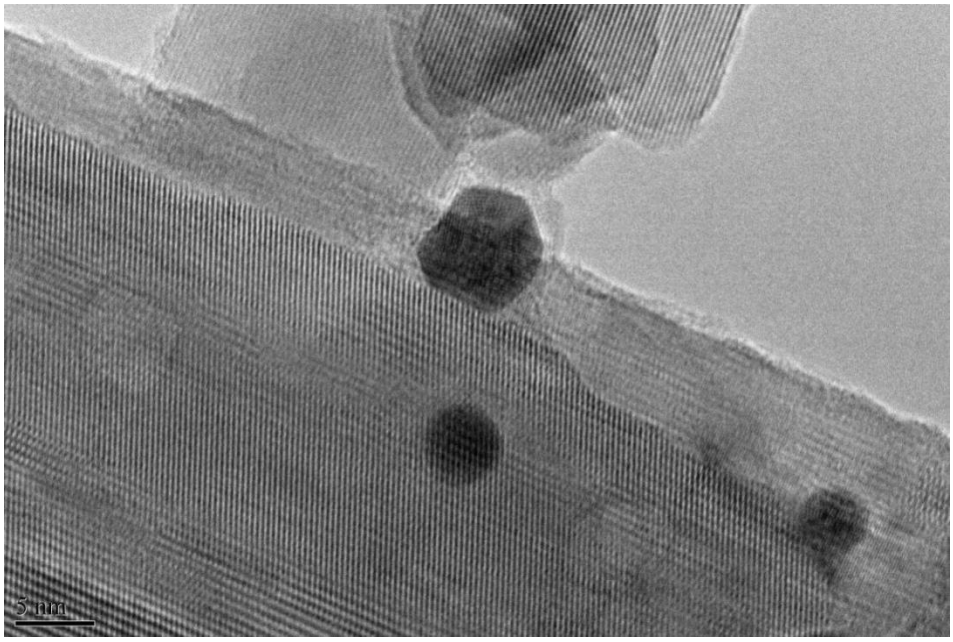

Fig. 4.18 HR-TEM image of Au-TNB@RT

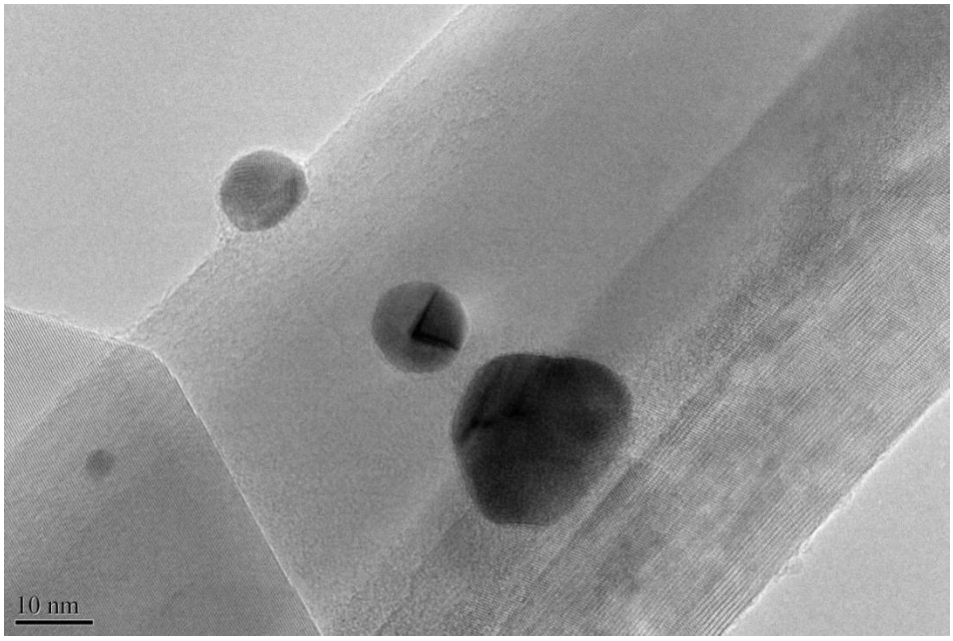

Fig. 4.19 HR-TEM image of Au-TNB@500C

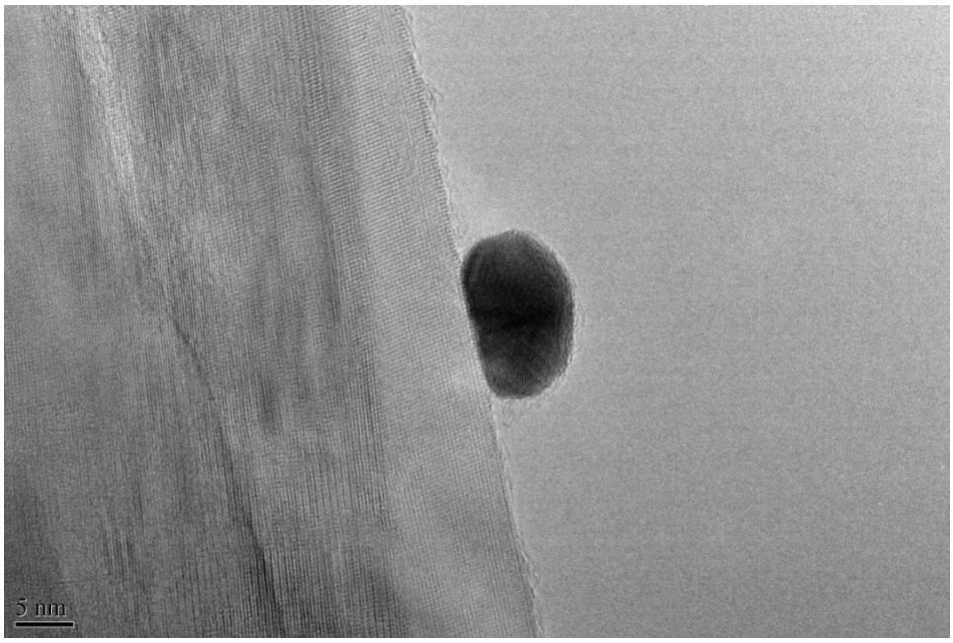

Fig. 4.20 HR-TEM image of Au-TNB@500C

4.2.3 UV-Vis spectra

UV-Vis absorption spectra of three samples are given in Fig. 4.21. Both Au-TNBs@RT and Au-TNBs@500C show greatly enhanced visible light absorption possibly due to the LSPR effect induced by Au nanoparticles. Various reports mentioned that Au nanoparticles have characteristic plasmon band around 500-550 nm, which is corresponded with our results [2, 3]. Au-TNBs@500C shows a red shift in the plasmon band, which is related to the size increase of Au nanoparticles.

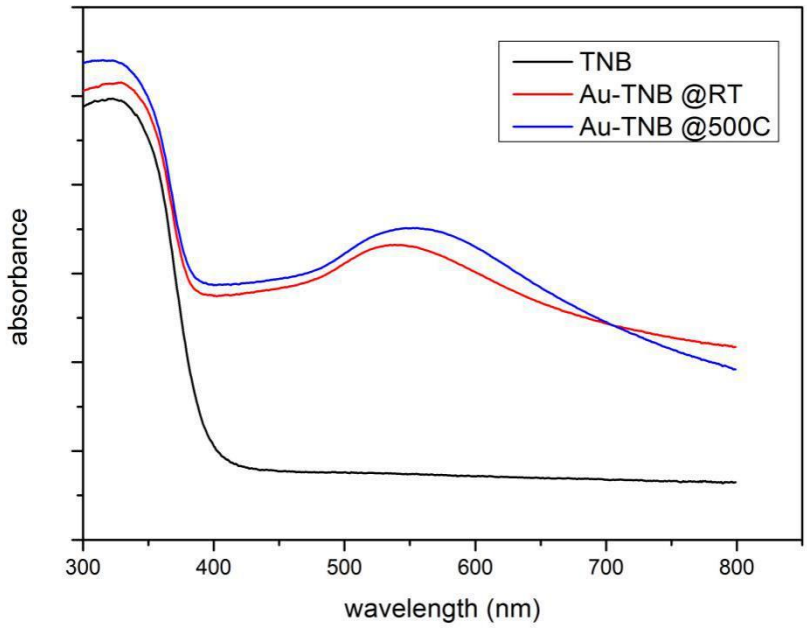

Fig. 4.21 UV-Vis spectra of TNBs, Au-TNBs@RT and Au-TNBs@500C

4.2.4 XPS photoelectron spectra

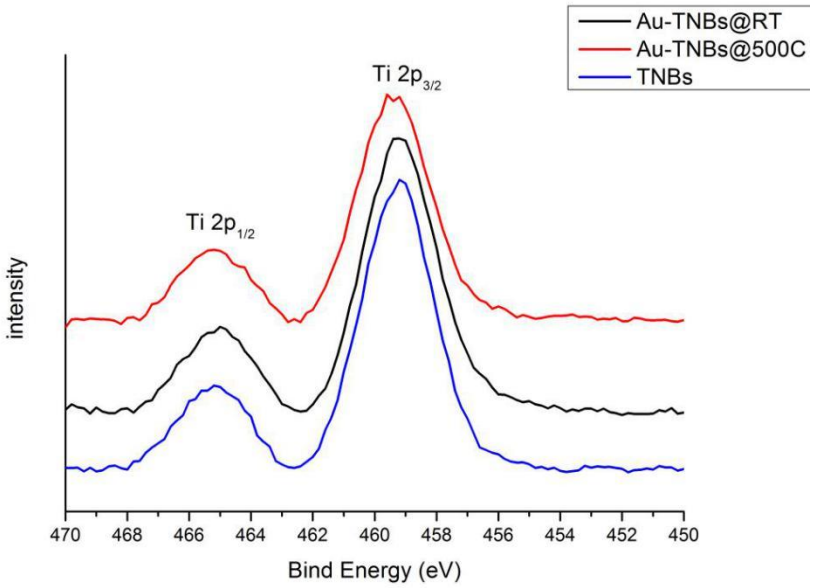

Fig. 4.22 XPS spectra of Ti (2p) in TNBs, Au-TNBs@RT and Au-TNBs@500C

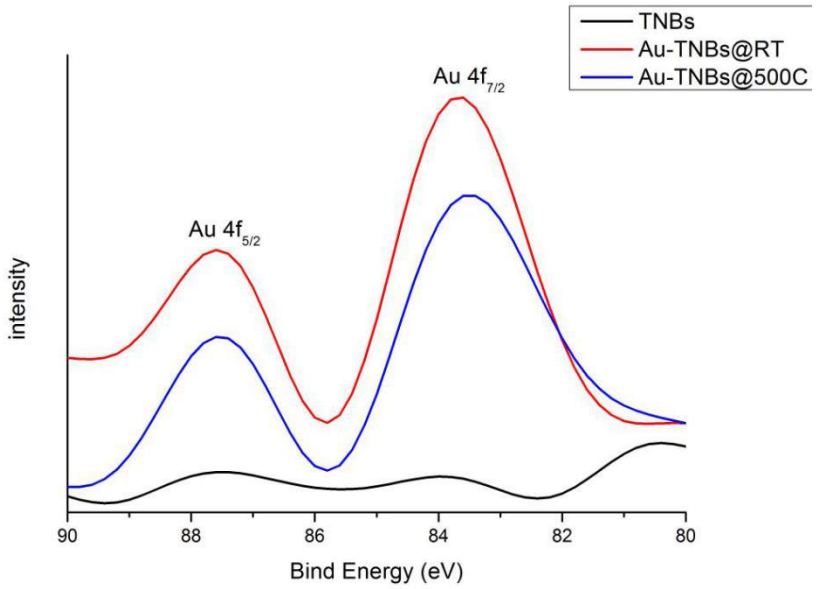

Fig. 4.23 XPS spectra of Au (4f) in TNBs, Au-TNBs@RT and Au-TNBs@500C

X-ray photoelectron spectroscopy is heavily used when detailed surface elemental information is needed. Fig. 4.22 and 4.23 display the XPS spectra of TNBs, Au-TNBs@RT and Au-TNBs@500C. Two peaks of Ti^{4+} can be observed: Ti $2p_{3/2}$ at 459.4 eV and Ti $2p_{1/2}$ at 465.1 eV respectively (Fig. 4.22). No significant peak shift happens to indicate that there is any change in electron state when Au is loaded. Au $4f_{7/2}$ and Au $4f_{5/2}$ can be observed for Au-TNBs (Fig. 4.23). It is noticeable that calcination have considerable impact on the energy of Au. The peak of Au $4f_{7/2}$ drop from 83.7 eV to 83.5 eV, and the peak of Au $4f_{5/2}$ drops from 87.6 eV from 87.5 eV.

4.2.5 MB degradation curves

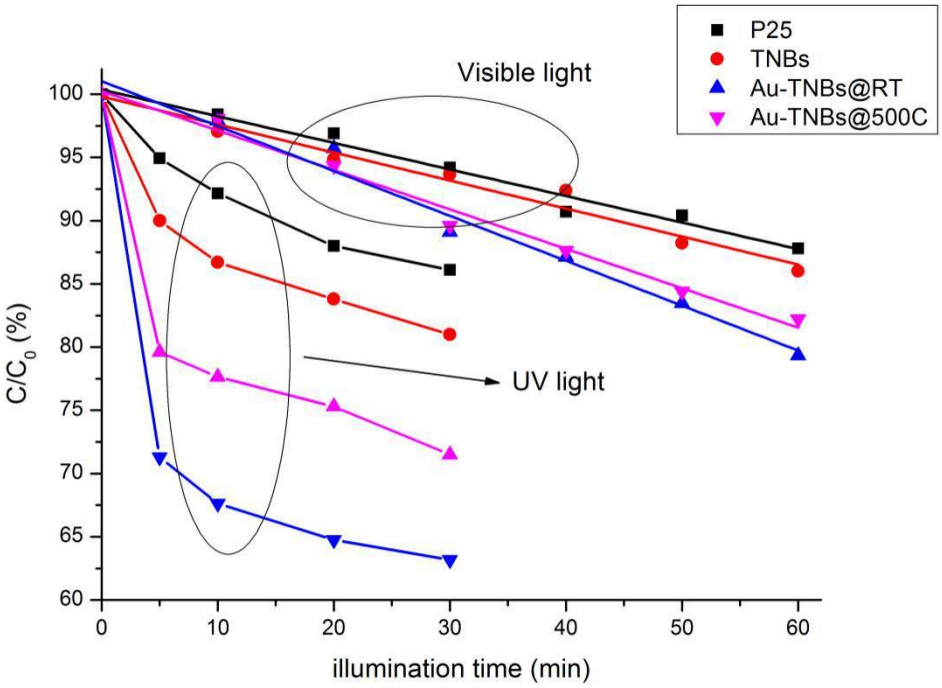

Fig. 4.24 MB degradation curve of P25, TNBs, Au-TNBs@RT and Au-TNBs@500C

MB degradation test was performed on P25, TNBs, Au-TNBs@RT and Au@TNBs@500C in order to compare their difference in photoactivity. Degradation curves are given in Fig. 4.24. Photocatalytic performance under different illumination condition was tested separately. While TNBs have better photoactivity than P25 under UV illumination as shown in the previous section, Au-TNBs can offer even better performance, possibly due to the more efficient charge separation and transportation induced by a Schottky barrier between Au and anatase TiO_2.

Chapter 5

CONCLUSION AND FUTURE WORK

In this thesis, a stirring-assisted hydrothermal synthesis is introduced, helping us successfully modify TiO_2, a very common photocatalyst, into a highly crystallized 1D nanomaterial: TNBs. The impact of stirring on the morphology and property of TNBs has been studied: Stirring with higher rotation speed can promote the anisotropic growth of anatase TNBs, leading to higher aspect ratio. This change may result in more exposed (001) facets in our TNBs, explain the superior photocatalytic performance under UV light. On the basis of TNBs, a heterogeneous photocatalyst is obtained: Au-TNBs. The loading of Au strengthen the light harvest efficiency significantly in the visible light range, overcoming a disadvantage of TiO_2, offering a potential application of TiO_2 photocatalyst in the commercial use.

Details about the growing mechanism and how rotation speed have impact on that are where our curiosity relies in. Reports mentioned about the formation of nanosheets during the early stage of hydrothermal synthesis and the split of these nanosheets after certain amount of time [13, 14]. However, these reports are obscure and do not study the mechanical influence of continuous stirring. The future work will also include further improvement of TNBs by loading other materials. For example, Fe-TiO2 is reported to be synthesized using hydrothermal method similar to us [23] and can be used as a potential catalyst for CO oxidation reaction [24].

References

[1] Fujishima, A. and K. Honda (1972). "Electrochemical Photolysis of Water at a Semiconductor Electrode." Nature 238(5358): 37-+.

[2] Pu, Y. C., et al. (2013). "Au nanostructure-decorated TiO2 nanowires exhibiting photoactivity across entire UV-visible region for photoelectrochemical water splitting." Nano Lett 13(8): 3817-3823.

[3] Qu, Y. and X. Duan (2013). "Progress, challenge and perspective of heterogeneous photocatalysts." Chem Soc Rev 42(7): 2568-2580.

[4] Abdelaal, M. Y. and R. M. Mohamed (2013). "Novel Pd/TiO2 nanocomposite prepared by modified sol-gel method for photocatalytic degradation of methylene blue dye under visible light irradiation." Journal of Alloys and Compounds 576: 201-207.

[5] Li, C., et al. (2009). "Preparation of Ni/TiO2 Nanoparticles and Their Catalytic Performance on the Thermal Decomposition of Ammonium Perchlorate." Chinese Journal of Chemistry 27(10): 1863-1867.

[6] Akhavan, O. (2009). "Lasting antibacterial activities of Ag-TiO2/Ag/a-TiO2 nanocomposite thin film photocatalysts under solar light irradiation." Journal of Colloid and Interface Science 336(1): 117-124.

[7] Li, Y., et al. (2014). "Preparation of Au-sensitized 3D hollow SnO2 microspheres with an enhanced sensing performance." Journal of Alloys and Compounds 586: 399-403.

[8] Suchanek, W. L. and R. E. Riman (2006). "Hydrothermal Synthesis of Advanced Ceramic Powders." Advances in Science and Technology 45: 184-193.

[9] Houas, A., et al. (2001). "Photocatalytic degradation pathway of methylene blue in water." Applied Catalysis B-Environmental 31(2): 145-157.

[10] Zhang, T. Y., et al. (2001). "Photooxidative N-demethylation of methylene blue in aqueous TiO2 dispersions under UV irradiation." Journal of Photochemistry and Photobiology a-Chemistry 140(2): 163-172.

[11] Lachheb, H., et al. (2002). "Photocatalytic degradation of various types of dyes (Alizarin S, Crocein Orange G, Methyl Red, Congo Red, Methylene Blue) in water by UV-irradiated titania." Applied Catalysis B-Environmental 39(1): 75-90.

[12] Carp, O., et al. (2004). "Photoinduced reactivity of titanium dioxide." Progress in Solid State Chemistry 32(1-2): 33-177.

[13] Yuan, Z. Y., et al. (2002). "Titanium oxide nanoribbons." Chemical Physics Letters 363(3-4): 362-366.

[14] Yuan, Z. Y. and B. L. Su (2004). "Titanium oxide nanotubes, nanofibers and nanowires." Colloids and Surfaces a-Physicochemical and Engineering Aspects 241(1-3): 173-183.

[15] Lan, Y., et al. (2005). "Titanate nanotubes and nanorods prepared from rutile powder." Advanced Functional Materials 15(8): 1310-1318.

[16] Wang, J., et al. (2009). "Origin of Photocatalytic Activity of Nitrogen-Doped TiO2 Nanobelts." Journal of the American Chemical Society 131(34): 12290-12297.

[17] Linsebigler, A. L., et al. (1995). "Photocatalysis on Tio2 Surfaces - Principles, Mechanisms, and Selected Results." Chemical Reviews 95(3): 735-758.

[18] Sato, S. and J. M. White (1980). "Photo-Decomposition of Water over Pt-Tio2 Catalysts." Chemical Physics Letters 72(1): 83-86

[19] Ohsaka, T. Journal of the Physical Society of Japan 1980, 48, (5), 1661-1668.

[20] Khan, M. M., et al. (2012). "Enhancement in the Photocatalytic Activity of Au@TiO2 Nanocomposites by Pretreatment of TiO2 with UV Light." Bulletin of the Korean Chemical Society 33(5): 1753-175

[21] Tian, F., et al. (2012). "Raman Spectroscopy: A New Approach to Measure the Percentage of Anatase TiO2 Exposed (001) Facets." The Journal of Physical Chemistry C 116(13): 7515-7519.

[22] Selloni, A. (2008). "Crystal growth - Anatase shows its reactive side." Nature Materials 7(8): 613-615.

[23] Nguyen, V. N., et al. (2011). "Hydrothermal synthesis of Fe-doped TiO2nanostructure photocatalyst." Advances in Natural Sciences: Nanoscience and Nanotechnology 2(3): 035014.

[24] u, S., et al. (2012). "Preparation and characterization of Fe-doped TiO2 nanoparticles as a support for a high performance CO oxidation catalyst." Journal of Materials Chemistry 22(25): 12629.

Biographical Information

Yi Shen received his bachelor degree in Materials Physics from Sun Yat-sen University in 2013 and joined the department of Materials Science and Engineering of UTA in the same year. Under the instruction of Dr. Fuqiang Liu, Yi Shen focused mainly on the synthesis and modification of TiO_2, a commonly used photocatalyst. Working together with Dr. Chia-Jen Hsu, he developed a stirring-assisted hydrothermal method to tailor the size and morphology of TiO_2 in a simple non-thermodynamical way. One-dimensional anatase TiO_2 nanobelts aka TNBs were successfully obtained which show superior photocatalytic performance over commercial P25. Yi Shen performed a series of experiments involving nitrogen, sulfur and gold deposition onto TNBs to further improve the photoactivity. Au loading turned out to be successful in the end, and Au-TNBs which have great photocatalytic performance in both UV range and visible light range were obtained.